

---

# BREATHING PATTERN MONITORING USING REMOTE SENSORS

---

PREPRINT

Janosch Kunczik <sup>1</sup>, Kerstin Hubbermann <sup>1</sup>, Lucas Mösch <sup>1</sup>, Andreas Follmann <sup>1</sup>, Michael Czaplik <sup>1</sup>, and Carina Barbosa Pereira <sup>1</sup>

<sup>1</sup> Department of Anesthesiology, RWTH Aachen University, Faculty of Medicine, Aachen, Germany

19 September 2022

## ABSTRACT

Breathing is one of the most important body functions because it provides it with oxygen, which is vital for energy production. In addition, the removal of carbon dioxide actively regulates the acid-base level, which is essential for the physiological function of the body. Due to its close connection with many other body functions, respiration can also be used as an indicator for a wide spectrum of medical conditions, which at first glance have little to do with breathing. Neurological, cardiological, inflammatory, metabolic, and even psychological conditions symptomatically show up in breathing patterns. Hence, being able to classify them automatically and unobtrusively, can allow cost-effective monitoring systems to continuously assess the health of a patient. In this work, multiple respiratory signal-extraction algorithms for thermal and RGB cameras are presented and compared. A novel algorithm for the extraction of multiple respiratory features is presented and evaluated. Using a one vs. one multiclass support vector machine, these features were used to classify a wide range of respiratory patterns with an accuracy of up to 95.79 %.

**Keywords** contactless · classification · infrared thermography · RGB video · dataset · signal · extraction

## 1 Introduction

Respiration provides the most important information to assess a patient for potentially life-threatening conditions. Various algorithms in emergency medicine first call for verification and assurance of adequate breathing, before other diagnostic or therapeutic steps are to be taken [1, 2, 3]. Even the decision whether to resuscitate an unconscious patient is made only on the basis of whether spontaneous breathing is present. Respiration is responsible for supplying the body with oxygen, which is essential for energy production and thus the maintenance of body functions. Furthermore, the respiratory activity regulates the CO<sub>2</sub> levels by removing it during expiration, which directly influence the body's pH-levels. Hence, disturbances in these processes are directly life threatening, as all other body functions rely on them. As result, many critical problems can be firstly observed in the respiratory activity, before they manifest in other vital signs, such as heart rate, peripheral oxygen saturation or blood pressure. This is the reason why breathing plays such a vital role in emergency medicine.

Assessing respiration can not only give insight about critically important gas exchange, but can also be used as an indicator for a wide range of medical conditions. Traumatic injuries, cardiac, neurological, inflammatory, metabolic and psychological conditions often lead to distinct changes in the breathing pattern. Therefore, an automatized monitoring of respiratory activity can give valuable information about the patient's health state and could be used to prevent a wide spectrum of fatalities by allowing an early detection of these conditions.

The current state of the art for breathing pattern assessment utilizes respiratory belts strapped around a subjects chest. While this approach is feasible for clinical research and sleep labs, it is not suitable for long-term patient monitoring due to cumbersome cables. Hence, contactless assessment of respiratory patterns would be desirable as it would allow monitoring a broad range of patients on ordinary wards in hospitals, in nursing homes and even at home for possible life threatening conditions.

## 1.1 State of the Art and Scope of this Work

Multiple approaches have been published, which allow a contactless extraction of the Respiratory Rate (RR) [4]. Most of the approaches found in the literature utilize RF-based methods, such as radar, WiFi, or software defined radios. Camera based approaches using RGB, Infrared Thermography (IRT), and Near Infrared (NIR) are also very common. However, apart from some pure frequency considerations, the classification of different breathing patterns has not been shown, yet. Rehman et al. [5] stated that a respiratory pattern classification based on software defined radio measurements is possible and presented classifiers with good accuracy. However, as the description of the study protocol was kept very brief and the recorded dataset was not published, it can not be confirmed that the good classifications results are not mostly based on a sufficient separation in frequency between the different patterns and overfitting. Romano et al.[6] and Barbosa Pereira et. al. [7] both performed a study in which multiple subjects were asked to breath following a on-screen animation with different respiratory patterns. The experiments were recorded with RGB and IRT cameras, respectively. The data was then used to validate and compare multiple respiratory signal extraction algorithms against a gold standard by means of RR extraction quality. However, a classification of the different breathing patterns was not tried. Additionally, while many works in the past have extracted respiratory signals from IRT-, RGB- videos, or a combination of both, to the authors' knowledge, there is no work that directly compares the signal qualities obtained from both modalities.

Therefore, this work presents the results of a subject study, which was conducted similarly to the aforementioned studies, but while capturing the experiments with both, IRT, RGB cameras and respiratory belts. The recordings were augmented to cover the whole range of expected respiratory patterns, in order to prevent overfitting. Subsequently, different signal extraction algorithms of all modalities were compared against each other to determine the best modality and extraction algorithm for contactless respiratory pattern classification. Furthermore, a robust extraction algorithm for multiple respiratory features is presented and evaluated. Lastly, a classifier is proposed, which is capable of distinguishing between all respiratory patterns with an accuracy of up to 95.79 %.

## 1.2 Respiratory Patterns

In particular, medical textbooks contain descriptions of all breathing patterns (see e.g. [8, 9, 10, 11]). However they often contradict each other, so that this section shall be used to define and motivate the breathing patterns discussed in this publication.

Normal respiration is called eupnea and is defined by nearly sinusoidal thorax movements with RR between 12 and 18 Breaths/min [12]. Tachypnea, which is characterized through higher RR than for eupnea, can be caused by either an increased oxygen demand (e.g. during exercise or fever), a reduced gas exchange capability (e.g. through asthma, pneumonia, pulmonary embolisms, etc.), or an oversupply of  $\text{CO}_2$  through e.g. metabolic acidodsis. The reasons for tachypnea can also cause a similar phenomenon, in which instead with increased frequency the body copes with an increased Respiratory Effort (RE) (deeper breaths), which is then called hyperpnea. Because the three patterns are closely linked to each other, Hyperpnea is often synonymously referred to as Kussmaul breathing or hyperventilation, which is not entirely correct. Following the original publication from Kussmaul [13], his discovered pattern is defined by deep, laboured breaths with increased frequency, which can be seen in patients with severe metabolic acidosis. Hence, Kussmaul breathing is a combination of hyperpnea and tachypnea. Hyperventillation, often a sign for psychological conditions, like anxiety is defined through a pathologically high gas exchange, which can be caused by tachypnea, hyperpnea or a combination of both. Figure 1 shows this interaction between different breathing patterns. Hypoventilation on the other side, is often caused by bradypnea, or hypopnea, which are defined by lower RRs or REs, respectively. However, in contrast to hyperventilation, it can be also caused a reduced gas exchange an manifest itself in tachy- or hyperpnea. Hence, there are exceptions to the color scheme in Figure 1.

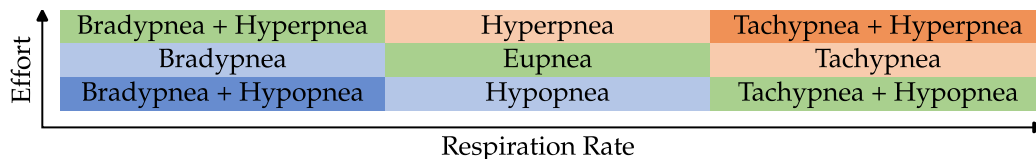


Figure 1: Qualitative respiration rate- and depth-based pattern differentiation: Hyperventilation and hypoventilation are marked by saturations of orange and blue, respectively. The more saturated the color, the more pronounced the condition.

Breathing is controlled by the respiratory center, which is located in the brain stem as part of the autonomic nervous system. Because the respiratory center is located near the narrow cranio-cervical junction, where the spinal cord leaves

the cranial cavity, it can be disturbed by increased intracranial pressure, traumatic brain injuries and through Meningism (inflammation of the protective membranes of the spinal cord). Intoxications can also influence its functions. All the aforementioned conditions can reduce its activity and thus lead to bradypnea, and hypopnea which can even develop into respiratory arrest (apnea). Strong impairments of the respiratory center manifest themselves as a pathological pattern called Biot’s breathing, which is characterized by periods of sufficient breathing, which are randomly interrupted with phases of apnea. An oxygen deficiency of the brain stem, for example due to a stroke or heart attack can yield a breathing pattern called Cheyne-Stokes which is like Biot’s breathing defined by intermitted phases of apnea, but with increasing and decreasing REs. A visual representation of all discussed respiratory patterns can be found in Figure 3. Since this work aims to classify respiratory patterns by video-based approaches, which can only capture changes in RR and RE, ventilation based patterns, like hyper- and hypoventilation weren’t further discussed.

## 2 Materials and Methods

### 2.1 Data Collection

Training and validation data was collected by means of a voluntary subject study with 10 male and female subjects aged 24 to 45 years. During a 15 minutes long recording, all subjects were asked to sit comfortably in the provided chair and to breathe according to the predefined breath-patterns. In advance, each subject was informed about the exact purpose and procedure of the study. Furthermore, it was expressly pointed out that the test protocol only needs to be followed at one’s own discretion. All subjects were informed that they could interrupt the experiment at any time, if e.g. breathing patterns were causing discomfort of any kind. The study was conducted after notification of the Ethics Committee of the University Hospital RWTH Aachen University.

Data was collected as shown in Figure 2 using three different sensor modalities. Two respiratory belt sensors, placed around thorax (1) and abdomen (2) of the subject served as gold standard reference signal sources. A RGB- and a IRT camera (5) were used to record the upper body of the sitting subject. To ensure proper illumination, a ring light (4) was placed between the subject and the cameras. Animations of the pre-defined breathing patterns were displayed on a computer (3) in front subject. MATLAB [14] was the software used for data collection and all evaluation. Detailed information about the used devices can be found in 5.



Figure 2: Experimental setup: A voluntary subject is sitting in a chair, wearing two RE sensors around thorax (1) and abdomen (2). A computer (3) displays predefined breathing patterns and stores the video frames of an RGB and LWIR camera (5). Illumination is ensured using a ring light (4).

The sequence of predefined breathing patterns is shown in Figure 3. It is henceforth referred to as **reference** signal, as it was used to compare all other modalities against it. A detailed description of the used patterns can be found in table 6. The protocol was designed and tested to alternate the different patterns such that, on average a normal gas exchange occurs. After each pattern, a five second pause was added, in which the subjects could breathe freely.

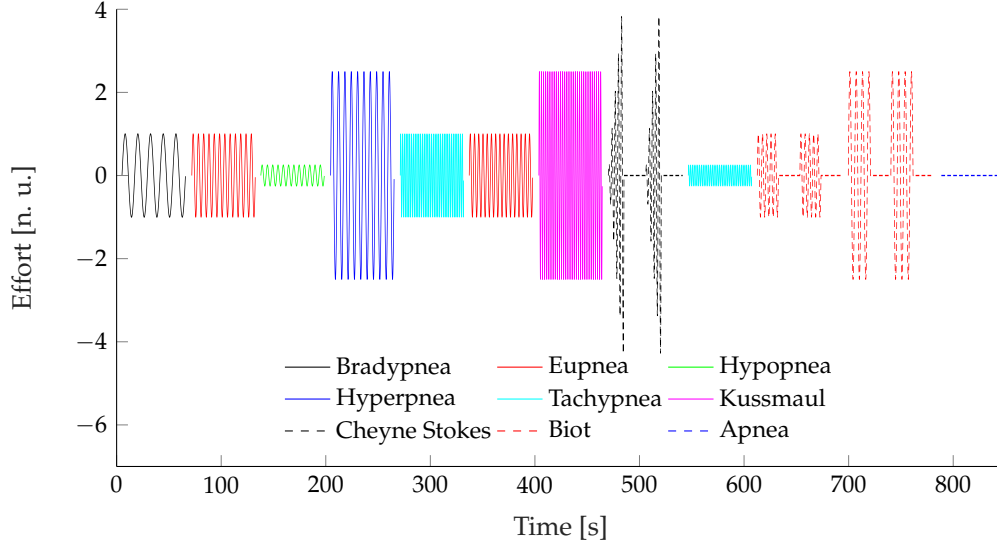


Figure 3: Visual representation of the breathing-pattern protocol.

## 2.2 Reference-signal Extraction

The readings from chest and abdomen belt sensors were over-sampled with 5 kHz, digitally low-pass filtered using a moving mean filter and then down-sampled to  $f_s = 10$  Hz. The extracted signals, from here on referred to as **chest belt** and **abdomen belt**, were used as gold standard references to determine the performance of their contactlessly extracted counterparts.

## 2.3 Raw RGB Signal Extraction

Respiratory signal extraction from RGB footage was achieved by tracking the motion subjects chest. For this purpose, 50 feature points were selected from this region, using the minimum eigenvalue algorithm [15]. These points were used to set-up and run a Kanade-Lucas-Tomasi (KLT) tracker [16, 17] (see Figure 4a), which tracked their positions in cartesian coordinates over the full length of the video. To transform the  $n$  individual, two-dimensional trajectories  $\mathbf{T}_i \in \mathbb{R}^{m \times 2}$ ,  $i \in [1, n]$  with length  $m$  into one-dimensional signals, a Singular value decomposition (SVD) was utilized:

$$\mathbf{T}_i = \mathbf{U}_i \mathbf{\Sigma}_i \mathbf{V}_i^*. \quad (1)$$

The SVD is a generalized form of the eigenvalue decomposition for non-square matrices and uses two change-of-basis matrices  $\mathbf{U}_i \in \mathbb{R}^{2 \times 2}$ ,  $\mathbf{V}_i^* \in \mathbb{R}^{m \times m}$  to rotate the signal's vector space, such that the semi-major and semi-minor axes of an ellipse, fitted to the signal distribution align with the coordinates systems base vectors. In the existing case,  $\mathbf{U}_i$  and  $\mathbf{V}_i^*$  represent base change matrices for the spatial and temporal domains, respectively. This allows for an reduction of the trajectories spatial dimensionality to only their main direction of motion, by mutliplying them with the first column vector of  $\mathbf{U}_i$ , called  $\vec{u}_{i,1}$ :

$$\vec{o}_i = \mathbf{T} \cdot \vec{u}_{i,1}. \quad (2)$$

The results were collected in the observation matrix  $\mathbf{O} \in \mathbb{R}^{m \times n}$

$$\mathbf{O} = [\vec{o}_1 \quad \dots \quad \vec{o}_i \quad \dots \quad \vec{o}_n], \quad (3)$$

which is composed by  $n$  trajectories  $\vec{o}_i \in \mathbb{R}^m$ ,  $i \in [1, n]$  with length  $m$ . These signals are referred to in the following as **chest RGB**.

## 2.4 Raw Thermal Signal Extraction

The respiratory signal extraction from thermal videos was performed using three independent approaches:

- observation of temperature changes below the nostrils (referred to as **nose IRT**),
- tracking the subject's upper body movement in contrast to the background (referred to as **border RoI**) and



(a) Spatially equally distributed minimum eigenvalue feature points on subject's chest (b) Region of interest for IRT videos: at border between subject and background (yellow) and around the subject's nose

Figure 4: Points and regions of interest for respiratory signal extraction for color and thermal videos.

- tracking of feature point on the subjects chest, analog to the RGB-based approach in section 2.3 (referred to as **chest IRT**).

The first approach was investigated in multiple publications [18, 19, 20] and is based on the fact that inspiration cools and expiration warms the nostrils. Hence, their temperature change can be used as respiratory signal. To extract the nostril temperature, a Region of Interest (RoI) around the subject's nose was selected (see Figure 4b) and tracked using minimum eigenvalue [15] feature points in the subject's face and a KLT tracker [16, 17] (see Figure 4). The RoI's mean temperature was extracted in every frame and was directly used as respiratory signal  $s[k]$ .

For the second approach, the high natural contrast between the subject and the background was used. The first recorded thermal frame was automatically segmented into foreground and background, using Otsu's method [21]. Subsequently, all regions in the foreground mask were ordered by their area. The region with the largest area was treated as a mask for the test subject. To extract respiratory signals, a number of  $n = 30$  RoIs with a size of  $25 \times 25$  pixels were initialized along the border of the test subject and the background (see Figure 4b). Their mean value was computed for every frame of the video and again saved in an observation matrix  $\mathbf{O}$ . To make the signal extraction robust against larger movements of the test subject, the two-norm of the difference of all consecutive frames was computed:

$$e_{m,k} = \|\mathbf{O}_k - \mathbf{O}_{k-1}\|^2. \quad (4)$$

If the motion error  $e_{m,k}$  grew larger than 5, the frame was marked as unusable and discarded. Two seconds after the latest, marked frame, all RoIs were re-initialized and the signal extraction was continued.

## 2.5 Robust Respiratory Signal Extraction

Not all signals in the observation matrices  $\mathbf{O}$  are mainly influenced by the subject's respiratory activity, but may also contain motion artifacts or only consist of noise. These signals can not be used for a robust respiratory signal extraction and thus should be discarded. To decide which signals are suitable, the correlation matrix  $\mathbf{P}$  of  $\mathbf{O}$  was computed. It was assumed that the respiratory activity yields a high correlation between all signals in which it can be observed. Thus, the mean correlation between a signal and all other observed signals was calculated:

$$\rho_{\mu,i} = \sum_{j=1}^n \frac{\rho_{j,i}}{n}, i \in [1, n]. \quad (5)$$

Only the five signals with the biggest mean correlation coefficient were kept in a reduced observation matrix  $\mathbf{O}_{max}$ , which was then used as input for a moving window Principal component analysis (PCA) with a window length  $w_l$  of 30 s:

$$\mathbf{C}_k = [\vec{c}_1, \dots, \vec{c}_5] = PCA(\mathbf{W}_k \cdot \mathbf{O}_{max}). \quad (6)$$

The window matrix  $\mathbf{W}_k = \mathbb{1}_{\{1, \dots, k-1, k+w_l, \dots, m\}} \in \mathbb{R}^{w_l, n}$  is a submatrix of a  $m$ -dimensional identity matrix, which only selects the observation points  $[k, k + w_l - 1]$  and thus only provides a portion of the observation matrix to the PCA algorithm.

A PCA is an orthogonal, linear, transformation, which transforms the data into a new coordinate systems, where the first axis corresponds to the direction of the greatest signal variance. Since the variance of a signal is independent of its sign, the transformation-coefficients  $\mathbf{C}$  may change their sign for every move of the window, which causes discontinuities in the result. To resolve this problem, the signs of the current coefficient matrix  $\mathbf{C}_k$  were adjusted, to be identical to its predecessor, using the direction matrix  $\mathbf{D}_k$ :

$$\mathbf{D}_k = \text{sgn}(\mathbf{C}_k \circ \mathbb{1}) \cdot \text{sgn}(\mathbf{C}_{k-1} \circ \mathbb{1}), \quad (7)$$

where  $\circ$  is the Hadamard product. Finally, the robust respiratory signal  $s[k]$  at time  $k$  could be computed by multiplying the observation vector  $\vec{o}_k$  with the direction matrix  $\mathbf{D}[k]$  and the first column vector  $\vec{c}_{1,k}$  of the coefficient matrix  $\mathbf{C}[k]$ , which represents the signal's principal component:

$$s[k] = \vec{o}_k \cdot \mathbf{D}_k \cdot \vec{c}_{1,k}. \quad (8)$$

## 2.6 Dataset Creation

After the respiratory signal extraction from all aforementioned modalities and approaches, the sequences were manually labeled by comparing them with the reference signal. Because for different modalities and different subjects, the signal amplitudes varied noticeably, all signals were normalized. For this purpose, the signal amplitudes in phases with apnea were calculated by finding the maximum amplitude in their Fast Fourier Transform (FFT) spectrum. These amplitudes were defined to have the value 1 normalized unit (n.u.):

$$s_{norm}[k] = \frac{1}{\max(|\mathfrak{F}(\vec{s}_{eup})|)} \cdot s[k]. \quad (9)$$

It was noted that all signals exhibited a slight systematic error in their sampling rate. Therefore, all signals of a modality were resampled to match the desired sampling rate and were then aligned with each other by finding the most likely delay  $d_{i,j}$  between every signal pair, using their cross correlation. Using a least squares optimization problem of the form

$$\begin{bmatrix} d_{1,2} \\ \vdots \\ d_{i,j} \\ \vdots \\ d_{n-1,n} \end{bmatrix} = \begin{bmatrix} 1 & -1 & \cdots & & 0 \\ & & \vdots & & \\ 0 & \cdots & 1 & \cdots & -1 & \cdots & 0 \\ & & & \vdots & & & \\ 0 & & \cdots & & -1 & 1 \end{bmatrix} \begin{bmatrix} d_1 \\ \vdots \\ d_i \\ \vdots \\ d_n \end{bmatrix}, \quad (10)$$

these distances were converted into the specific signal offsets  $d_i$ . Some signals exhibited a larger error in their sampling rate and were discarded in the first resampling and alignment step. To match those signals with the rest, a grid search over all possible resampling factors was performed. The factors that yielded the highest cross correlation value and their corresponding lag were chosen to resample and delay these signals accordingly. The dataset was then stored in the MIT Waveform Database (WFDB) format.

To augment the dataset, the original data was altered by combining arbitrary signals  $s_i[k]$  and  $s_j[k]$  of different subjects, with each other using random percentages  $p \in [0, 1]$ :

$$s_{gen,l}[k] = p \cdot s_i[k] + (1 - p) \cdot s_j[k]. \quad (11)$$

Afterwards, the signals  $s_{gen,l}[k]$  were split into the individual, recorded breathing patterns. For each breathing pattern, the signal was either stretched, or compressed to randomly vary the RR within its specified target range (see 6). Through this approach, the original dataset size was increased to 1000 samples for each pattern, modality and extraction approach, to allow the utilization of arbitrary machine learning classifiers. Furthermore, the RR of the recorded signals was randomly distributed to prevent classifiers from simply distinguishing several patterns through their distinct frequency. Because the required RE of the recorded Kussmaul breathing pattern could not be replicated by any subject (see Figure 5), those sections were discarded and replaced with hyperpnea patterns that were shifted into the higher Kussmaul RR range.

## 2.7 Feature Extraction

In a pre-processing step, the respiratory signals  $s[k]$  were smoothed by filtering with a Savitzky-Golay filter [22] with the parameters shown in table 7. Using MATLABs finpeaks algorithm, all peak locations  $T_p[k]$ , their amplitudes  $a[k]_{p,nu} = 0.5 \cdot p[k]$  (where  $p[k]$  is the peak prominence) and half-widths  $w[k]_{p,nu}$ , which fulfilled the criteria given in table 8 were extracted from the smoothed signal.

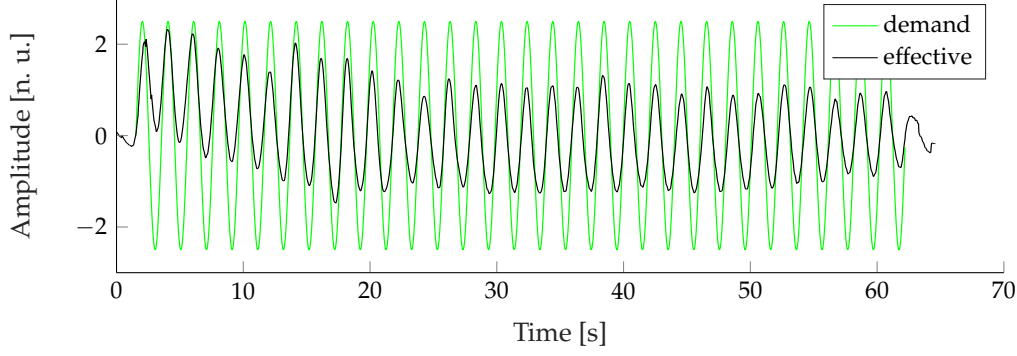


Figure 5: Kussmaul pattern excluded from dataset, because of big difference between demanded respiratory activity and the mean effective respiratory response of all subjects.

The RR was computed through the inverse of the continued differentiation between two consecutive peak locations  $T_{p,k}$  and  $T_{p,k-1}$ :

$$RR_{p,nu}[k] = \frac{60}{T_{p,k} - T_{p,k-1}}. \quad (12)$$

Because  $RR_{p,nu}[k]$ ,  $A_{p,nu}[k]$  and  $w_{p,nu}[k]$  are non-uniformly sampled with the occurrence of the inspiratory peaks, they were re-sampled into  $RR_p[k]$ ,  $A_p[k]$  and  $w_p[k]$  to match the length and sampling rate of  $s[k]$ , using a next neighbour interpolation, which holds the last detected value until the next value.

To increase the robustness of the feature extraction, the RR and its amplitude were also extracted from the signal's spectrum using Continuous Wavelet Transform (CWT) ridges. Ridge points represent the local maxima of a spectrogram and indicate a signal's instantaneous frequencies and amplitudes within the resolution of the used transform [23]. Hence, the RR and the respiratory amplitude were computed from continuous wavelet spectrogram  $S[f, k]$  of  $s[k]$  by finding the frequency  $f \forall k$ , which maximizes the value of  $S$ :

$$\begin{aligned} RR_S[k] &= 60 \cdot \arg \max_f (S[f, k]), \\ A_S[k] &= \max_f (S[f, k]). \end{aligned} \quad (13)$$

The parameters used to compute  $S[f, k]$  can be found in 9. A CWT spectrogram with its ridge signal is shown in Figure 6.

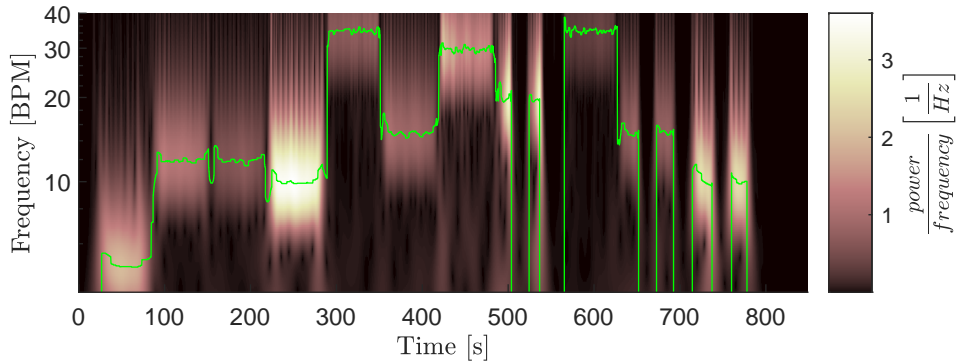


Figure 6: Continuous wavelet spectrum of the mean RGB signal, including the extracted Respiratory Rate.

## 2.8 Artifact Correction

Artifact correction was done on both feature tuples  $F_p[k] = (RR_p[k], a_p[k], w_p[k])$  and  $F_s[k] = (RR_S[k], a_S[k])$  individually. For the ease of notation, the following equations are thus derived from a generic feature set  $F_i[k]$   $i \in [p, S]$ .

Signals segments that were too discontinuous, showed noisy behavior below a certain respiratory amplitude, had a too low RR, or contained too few valid values, were invalidated. To remove segments with too many discontinuities in

RR, all steps greater than 5 Breaths/min were marked. If two discontinuities occurred within a 10 s time frame, the associated section was discarded.

Signals with amplitudes below 0.05 n.u. were marked as unreliable. In order to include the associated segments anyway, three conditions had to be met: the segment  $F_{i,j} \subset F_i$  had to be longer than five times the period length of its median RR, the median RR had to be greater than 5 Breaths/min and the onto the median RR normalized difference between the smallest and largest RR had to be smaller than 0.45 n.u.:

$$\begin{aligned}
 RR_{\text{med}} &= \widetilde{RR}_{i,j}[k], \\
 \text{length}(F_{i,j}[k]) &\geq \frac{5 \cdot 60}{RR_{\text{med}}}, \\
 &\text{in [s]} \\
 RR_{\text{med}} &> 5 \text{ Breaths/min}, \\
 \frac{\max(RR_{i,j}[k]) - \min(RR_{i,j}[k])}{RR_{\text{med}}} &> 0.45.
 \end{aligned} \tag{14}$$

Lastly, all segments, shorter than 10 s, were invalidated, as well. All invalid segments shorter than 10 s were subsequently filled with a moving median interpolation of the last five valid values. Segments not satisfying this condition were set to zero.

## 2.9 Robust Feature Fusion

Figure 7 shows the the peak- and CWT-ridge-based feature sets next to its underlying respiratory signal (Figure 7a). Though both sets were artifact corrected, it can be seen that they still exhibit some artifacts, independently from each other (For example between 100 - 300 s in Figure 7b). Generally, it has been observed that the temporally extracted feature set was more reliable during highly transient conditions, like during Biot's breathing and that the CWT-ridge method performed better in low amplitude scenarios, like during tachy- and hypopnea.

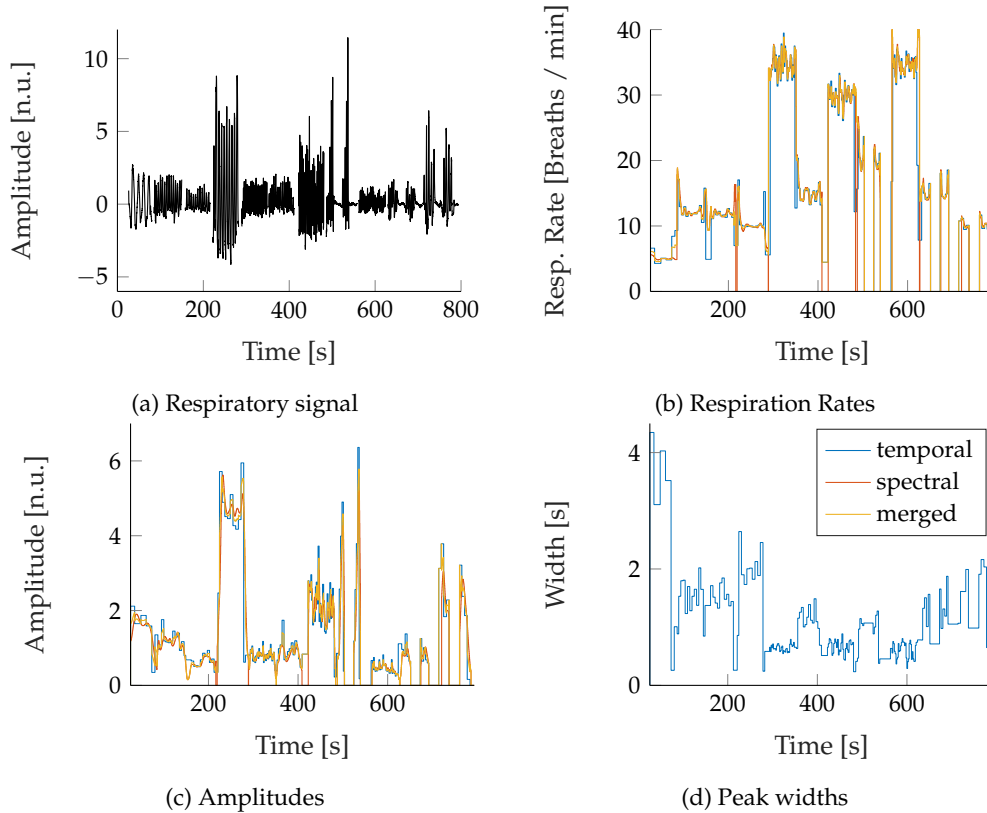


Figure 7: Time progression of the extracted features of an exemplary signal (RGB video of subject 6). All spectral, temporal and robustly merged features are displayed.

Hence, the results of both approaches were merged into a robust feature set. For this purpose, all signal jumps greater than 5 Breaths/min in the two respective RR were marked and used as segment borders. For each segment the, signals were merged with the following rules: If the difference between the median RR of both extraction approaches was smaller 3 Breaths/min, the mean of both signals was used. Else, the segment that had no signal jump in RR for at least 10 s and whose mean RR was higher compared to the other was used. If no valid section was present, the merged signal was set to an invalid value and later on filled using a moving median interpolation over the last 5 valid values and a maximum signal gap of 5 s. Values that were still invalid afterwards were set to zero. From the robust feature set, moving signal variances  $RR_{var}$  and  $A_{var}$  were computed with a time window of 30 s as a feature of change in the RR and RE.

## 2.10 Classification

For Breathing pattern classification a one vs. one multiclass Support Vector Machine (SVM) classifier was utilized. The input to the classifier were chosen to be the features with  $RR_{med}$  and  $A_{med}$   $RR_{var, med}$  and  $A_{var, med}$  computed by calculating their median over complete breathing pattern sections. SVMs were first introduced by Wapnik et al. [24] and are binary classifiers that optimize a linear border between two labeled classes, such that the distance of their datapoints to the border is maximized. To allow the classification of multiple classes, in the one vs. one approach proposed by Hastie et al. [25], a classifier for every combination of two classes is trained. The classifier was trained and validated using a 10-fold cross validation, in which the dataset was randomly split into 10 subsets, from which in every step 9 were used for training and one was used as validation data.

## 3 Results

### 3.1 Signal Extraction

Figure 8 visually compares the extracted respiratory signals, grouped by their origin modality, against the reference signal, to which all subjects adjusted their breathing during the recordings. The results of the nose IRT signal extraction approach are exemplary shown with the recordings of a single subject in Figure 8a. It can be seen that the signal is clearly oscillating with the reference, but no significant amplitude variations are visible. For this reason, the extraction approach was not further examined as detecting amplitude differences between the breathing patterns is crucial for their correct classification.

Figure 8b displays the remaining respiratory signal extraction approaches for IRT videos. The displayed signals represent the mean of all extracted signals over all recorded subjects. Regarding the frequency, an excellent agreement between both approaches and the reference signal can be observed. Clearly visible changes in amplitude during the different sections correlate well with the reference, but it can be seen that the signal amplitudes are visibly larger for the chest IRT approach during bradypnea and for the border RoI approach during hyperpnea. As the respiratory signals from RGB videos in 8c were extracted in the same way as the chest IRT signals, both are very similar to each other. Only during phases of apnea, the IRT-based signal seems to be less noisy. The border-based IRT signal on the other hand shows the most noise during those phases.

Visually the best accordance with the reference show signals extracted from the respiratory chest and abdomen belts in 8d. Here, the correlation between the signals frequency and amplitude are excellent. Only during phases of apnea, the belt-based signals performed noticeably worse, due to noticeable baseline wander.

### 3.2 Feature Extraction

Figure 7 in section 2.8 shows a high temporal resolution of the extracted respiratory features. It can be noted that the fusion of the two redundantly extracted feature sets reduces the artifacts in the merged feature set. The accordance between the RRs (Figure 7b) and REs (Figure 7c) is high, which implies a high certainty of the parameters. In signals with low REs, it could be noted that the CWT-ridge based approach performed much better than the peak detection approach, as single missed peaks altered the feature extraction result significantly.

Table 1 shows the Root Mean Square Error (RMSE) for the different respiratory breathing patterns compared to the reference signal, which all subjects were requested to follow breathing during the recordings. Therefore, the RMSE values do not only originate from the performance of the extraction algorithms alone, but are superimposed with the systematic errors the subjects made, while breathing according to the reference signal. However, since these errors influence all extraction approaches equally, the comparison between them still unveils their relative performance against each other. Regarding RMSE, the chest belt shows the best performance. Nevertheless, the previously observed inferior performance during respiratory arrest is also reflected in large error values in Biot's respiration and apnea. The

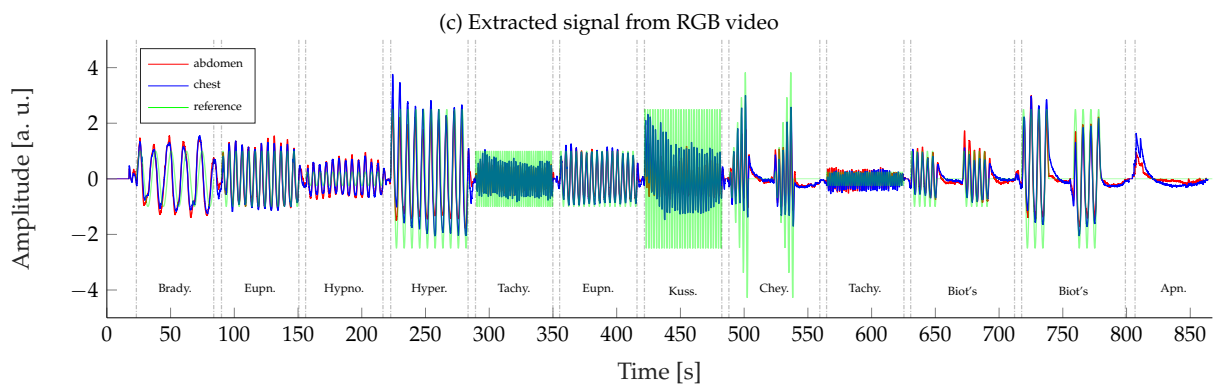
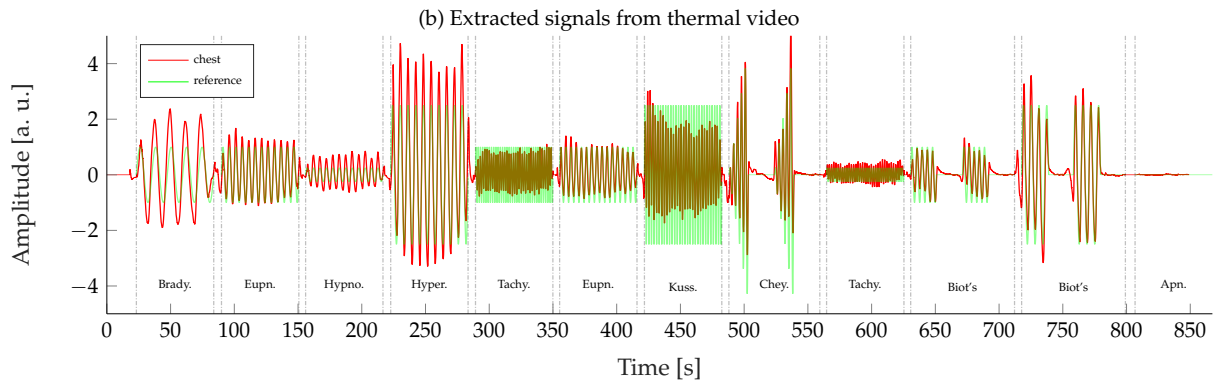
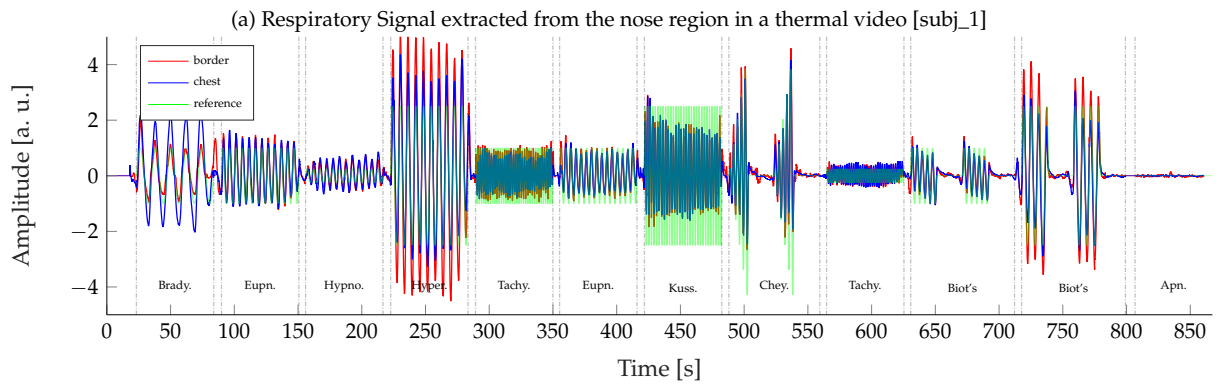
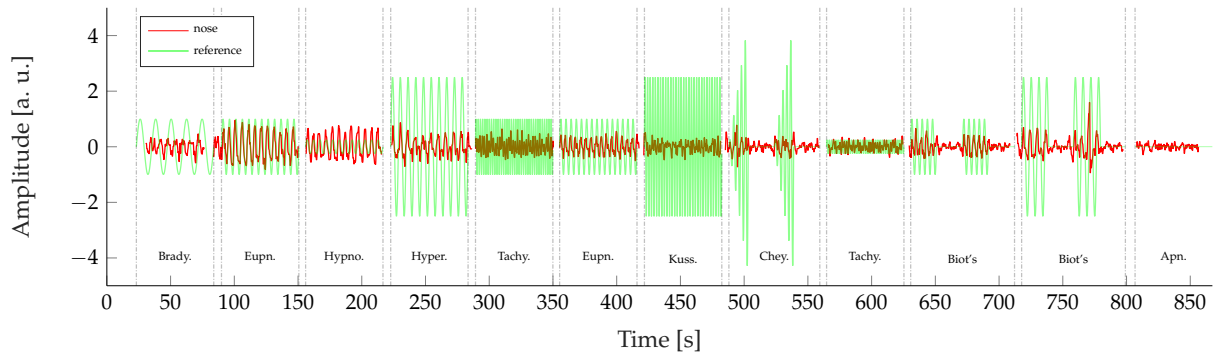


Figure 8: Temporal comparison of the mean signals of all modalities against the reference signal.

contactless modalities perform comparably well and show only slightly higher errors than the chest belt. However, due to the extremely high errors during phases of apnea for the chest belt signals, the mean RMSE of the contactless extracted signals outperforms the gold standard. The abdominally placed respiratory belt has the worst performance.

Table 1: Root-mean-square errors (RMSE) for the respiratory rate (RR) extraction of the different recorded breathing patterns and modalities. The unit of all values is in Breaths/min.

Pattern	Chest IRT	Border IRT	RGB	Abd. Belt	Chest Belt
Bradypnea	0,33	0,44	0,34	0,42	0,12
Eupnea	0,21	0,21	0,20	0,19	0,05
Hypopnea	0,28	0,36	0,28	0,24	0,10
Hyperpnea	0,21	0,14	0,13	0,24	0,05
Tachypnea	0,24	0,24	0,24	0,88	0,11
Kussmaul	0,40	0,28	0,29	0,37	0,14
Cheyne Stokes	0,56	1,61	0,86	0,88	0,23
Biot's	1,48	0,52	0,97	3,76	1,59
Apnea	0,00	0,60	1,20	7,43	6,20
<b>Mean</b>	<b>0,41</b>	<b>0,49</b>	<b>0,50</b>	<b>1,60</b>	<b>0,95</b>
<b>Median</b>	<b>0,31</b>	<b>0,40</b>	<b>0,32</b>	<b>0,65</b>	<b>0,13</b>

Figure 9 compares the contactless and the chest belt RR extraction against the reference signal using Bland-Altman plots. The respiratory rates of the animated reference signal  $RR_{ref}$  were used as ground truth. The errors during apnea phases were excluded. As in Table 1, it can be clearly seen that the median errors of the chest belt are significantly smaller. However, the Biot's breathing patterns between 12 and 25 Breaths/min introduce only few (see Table 2), but big outliers, which increase the overall standard deviation. Thereby, the standard deviations of all modalities and algorithms are very similar. The marker-based approaches show that the errors from RGB-videos are more equally distributed, while the IRT-based RR tend to have a smaller median error, but more outliers. The border ROI feature extraction approach shows the largest RR mean errors of all contactless modalities and has also the highest number of outliers (see Table 2). Interestingly, this approach produces the smallest median RMSE of all modalities and performs equally well as the gold standard (the chest belt signals), when comparing the amplitude errors as can be seen in Table 3. Except for patterns with high REs, as was seen before in Figure 8b, the errors are lower than for all other algorithms and modalities. Chest marker tracking in thermal videos also yields low amplitude errors, except for Biot's breathing and Bradypnea. Regarding amplitude errors, the chest RGB approach had the weakest performance.

Table 2: Outliers with errors greater than two standard deviations from the mean value for the respiratory rate (RR) extraction of the different recorded breathing patterns and modalities.

Pattern	Chest IRT	Border IRT	RGB	Abd. Belt	Chest Belt
Bradypnea	5	9	7	9	0
Eupnea	1	0	1	2	0
Hypopnea	1	3	3	0	0
Hyperpnea	0	0	0	1	0
Tachypnea	0	0	0	1	0
Kussmaul	0	0	0	0	0
Cheyne Stokes	2	10	2	3	0
Biot's	7	2	7	29	9
Apnea	0	9	13	210	209
<b>Sum</b>	<b>16</b>	<b>33</b>	<b>33</b>	<b>255</b>	<b>218</b>
<b>Ratio</b>	<b>0,18%</b>	<b>0,37%</b>	<b>0,37%</b>	<b>2,83%</b>	<b>2,42%</b>

### 3.3 Dataset Analysis

Figure 10 shows a plot matrix with the scatter plots of all extracted features by means of their median value over a complete breathing pattern segment. The respiratory width was excluded, as it did not provide a significant contribution

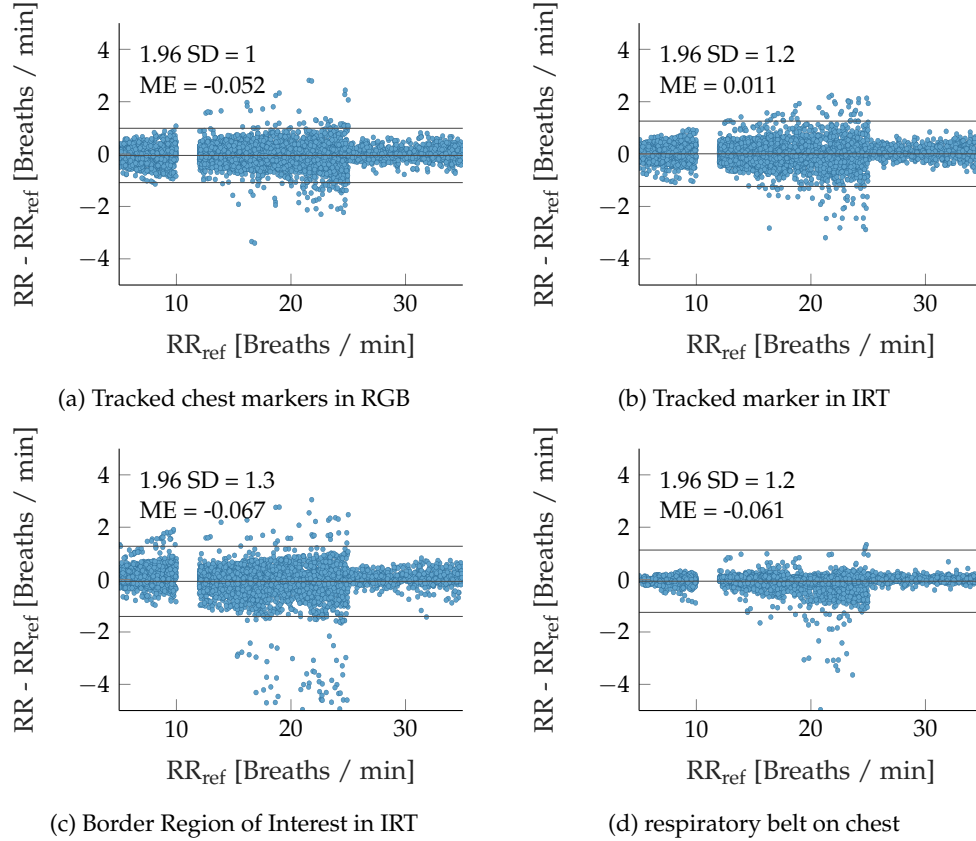


Figure 9: Bland-Altman diagrams for extracted respiratory rates.

Table 3: Root-mean-square errors (RMSE) for the respiratory amplitude extraction of the different recorded breathing patterns across all modalities. The unit of all values is in normalized units.

Pattern	Chest IRT	Border IRT	RGB	Abd. Belt	Chest Belt
Bradypnea	0,81	0,26	0,79	0,42	0,34
Eupnea	0,06	0,08	0,09	0,07	0,06
Hypopnea	0,29	0,27	0,36	0,37	0,35
Hyperpnea	0,73	2,57	1,86	0,94	0,77
Tachypnea	0,34	0,29	0,33	0,41	0,29
Kussmaul	0,64	2,26	1,66	1,06	0,83
Cheyne Stokes	0,84	0,85	0,95	1,14	0,90
Biot's	0,83	0,54	0,74	0,89	0,82
Apnea	0,00	0,01	0,00	0,02	0,01
<b>Mean</b>	<b>0,50</b>	<b>0,79</b>	<b>0,75</b>	<b>0,59</b>	<b>0,49</b>
<b>Median</b>	<b>0,57</b>	<b>0,42</b>	<b>0,75</b>	<b>0,51</b>	<b>0,42</b>

to the separation of the different respiratory pattern. Generally, no distinct lines can be observed in the feature distributions of  $RR_{med}$  and the signal amplitudes  $A_{med}$ . Instead, they are evenly distributed over the entire defined range of values. This confirms the effectiveness of the chosen data augmentation principles and prevents overfitting of classifiers at systematic gaps that would otherwise have arisen in the feature value ranges due to the study design.

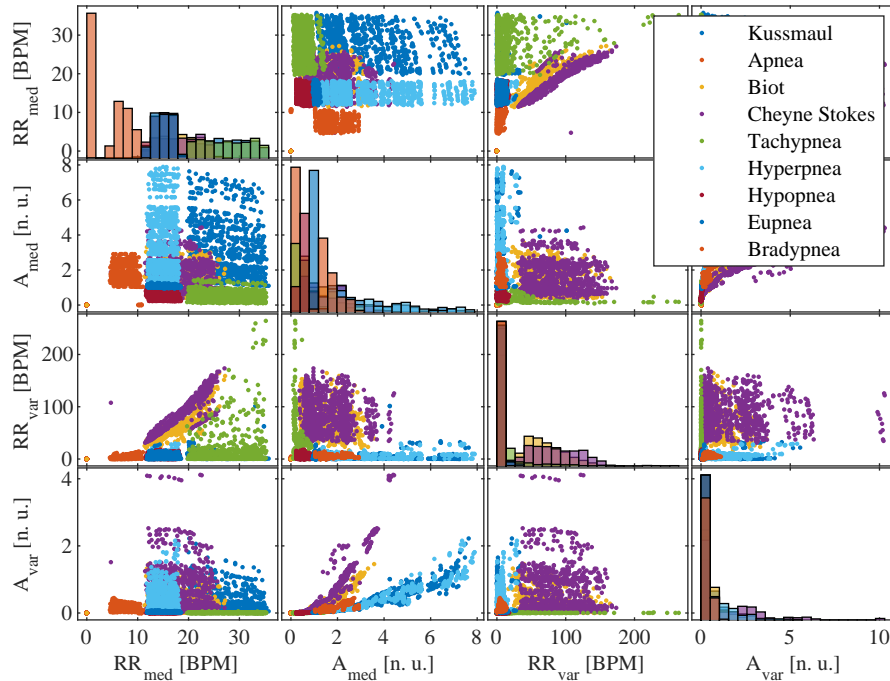


Figure 10: Scatter plots for all extracted respiratory feature combinations.

The histograms on the main diagonal of the plot matrix show the distribution of all classes along their complete value range. The RR is clearly the feature, which alone can provide the best separation between the displayed pattern classes. However, it is only sufficient for classification between apnea, bradypnea, eupnea and tachypnea. All other classes need multiple features for their extraction. Here, the most important pair of features appear to be the median RR  $RR_{med}$  and signal amplitude  $A_{med}$ , which show the RE. By adding this feature, also hypopnea, hyperpnea and Kussmaul breathing become separable. For complex respiratory patterns, like Biot's and Cheyne-Stokes breathing, which cover a wide range of RRs and REs, some separation between the other patterns can be established by introducing the variance features. Still, optically no clear separation can be achieved for these patterns.

### 3.4 Classification Results

The total classification for the different accuracies extraction algorithms and modalities are shown in Table 4. With almost 96 % accuracy, the chest marker tracking approach in IRT-videos outperformed the other approaches and even the chest belt, which serves as gold standard. Interestingly, all contactless approaches outperformed the gold standard, although it showed equal or better performance during the feature extraction.

Table 4: Breathing pattern classification results for all extracted signals using a one vs. one multiclass Support Vector Machine

	Chest IRT	Border RoI	Chest RGB	Abd. Belt	Chest Belt
<b>Accuracy</b>	95,79%	94,93%	93,48%	91,87%	92,37%

Figure 11 shows the confusion matrix of the respiratory signal extracted by chest feature tracking in IRT-videos. It can be seen that the results are almost perfect. The biggest source of confusion originates from the complex respiratory patterns (Biot's breathing and Cheyne Stokes respiration). With confusion rates of 1.3 % and 2.7 %, these breathing patterns were more than thirteen times more likely to be misclassified than hypopnea, the following largest source of confusion with 0.1 %.

Apnea	1000								11.1%	
Biot	3	880		110		2			9.8%	1.3%
Bradypnea			1000						11.1%	
Cheyne Stokes		246		754					8.4%	2.7%
Eupnea				1000					11.1%	
Hyperpnea					1000				11.1%	
Hypopnea				10		990			11.0%	0.1%
Kussmaul							1000		11.1%	
Tachypnea		3							11.1%	0.0%

Figure 11: Confusion matrix for the one vs. one multiclass Support Vector Machine breathing pattern classification of the respiratory signal extracted by chest feature tracking in thermal videos

## 4 Discussion

This work presented several approaches to extract and classify respiratory signals from RGB, or IRT videos. Their performances were compared to respiratory belt sensors, located at chest and abdomen, which served as gold standards. With the chest IRT approach, 95.79% classification accuracy was achieved. The other contactless approaches, border RoI and chest RGB performed comparably well and all outperformed the gold standard. These results are promising and clearly show the feasibility for contactless systems to perform a complete respiratory pattern assessment. As mentioned in the introduction, the knowledge over the current respiratory pattern can not only give insight into the patient's gas exchange, but can also be used as indicator for a broad range of medical conditions. Therefore, the relevance of a system, which is capable of continuously classifying a patient's respiratory pattern in an unobtrusive and cost-effective manner should not be underestimated.

Still, it should still be discussed which of the presented approaches is the most promising for a timely product development, where the performance differences in the different approaches come from, and which improvements, respectively extensions in the field of automated respiration analysis would be conceivable in the future. During evaluation, interesting differences regarding the quality of respiratory amplitude or RE extraction became apparent. Their reasons shall be discussed in the following: In contrast to the other modalities and measurement locations, the nose IRT signal was not able to show any differences in RE over the different breathing patterns. This is due to the fact that the temperature of the in- and exhaled air, which leads to temperature changes in the IRT recordings, does not vary with the RE, but with the respiratory flow. This renders it useless for the presented classification approach, but makes it very interesting for more advanced respiratory assessment approaches. For example, the monitoring of the relationship between flow and effort yields information about a lung's mechanical condition in terms of resistance and compliance. These two measures are vitally important when diagnosing obstructive, or restrictive lung diseases. The signals from the border RoI approach were inferior, compared to the chest-tracker-based approaches. This is due to the fact that for the latter approach more of the extracted raw signals contain relevant information, as they are all located on the subject's chest. Only around the shoulder regions, the border RoIs deliver signals with relevant respiratory content. This also explains the observed amplitude differences between the two approaches: while the chest-tracker-based approaches mainly evaluate chest rise, the border RoI approach focuses on shoulder movement. Healthy subjects increase their lung volume during phases of apnea (e.g. during meditation) to maintain a constant minute ventilation as compared to eupnea. This results in a larger chest excursion and thus larger signal amplitudes for the chest-tracker-based approaches. On the other hand, the border RoI approach is highly sensitive to the utilization of auxiliary respiratory muscles, which result in an additional lift of the shoulders. Hence, the border RoI signals had a significantly higher amplitude during phases with high RE. By simultaneously using the chest signals as surrogate for lung volume and the shoulder signals as surrogate for high REs, an even more fine-grained automatic assessment could be provided.

Also regarding the measurement modalities, there were notable differences, which shall be addressed in the following: In general, IRT has proven to be superior, compared to the other modalities. This can be explained by a high contrast of the subject against the colder background, but also on the subject's chest due to wrinkles in the clothing (see 4). Although RGB recordings have a higher resolution, the low contrast on single-colored textiles reduces the quality of the feature point tracking algorithm. Furthermore, over- and underexposure can further limit the usable contrast. However, there may exist scenarios, where IRT has less contrast than RGB sensors (e.g. outside during hot or cold weather, when

either the background has a similar temperature as the subject, or the subject wears insulated clothing). Because of the low cost of RGB sensors it is therefore proposed to use both modalities simultaneously and to perform signal fusion to further enhance the robustness. Chest belt sensors have shown to deliver high quality signals. However, during apnea, they were prone to artifacts due to baseline wander. In contrast to all other modalities, only one signal source was available and no implicit detrending through the PCA fusion algorithm could be performed. This fact contributed to the inferior performance during phases of apnea.

For breathing pattern classification, the contactless approaches outperformed the respiratory belts, although the chest belt signal showed better performance for RR and RE extraction. This can not alone be explained by the fact that respiratory belt signals showed inferior performance during phases of apnea. This fact contributed 0.1 % of false classifications to the overall performance. The main difference can be found in the error rates for classification of complex breathing patterns (Biots's breathing and Cheyne-Stokes respiration). Here, the contactless approaches performed better. A possible explanation might be that the contactless approaches tended to exaggerate high REs, which might be beneficial for classification. Nevertheless, because complex respiratory patterns consist of multiple simple patterns, one-shot classifiers, like the one presented in this manuscript are not perfectly suited for their classification. By using more advanced classifiers, there is the possibility that all discussed modalities yield the same results.

Multiple approaches could be tested to also accurately classify complex breathing patterns. The first possibility that the authors can think of would be to use the CWT spectrograms as inputs for a suitable 2D Convolutional Neural Network. This would provide the classifier with all relevant time-frequency and amplitude information, necessary for successful classification. Also, the temporal feature signals themselves could be used as input for a suitable recurrent neural network. The memory effect of these neural networks make them ideal for classifying temporal patterns. A last possibility would be to use the presented classifier in this paper only for the simple breathing patterns and to rely on a simple, downstream recurrent neural network to detect and classify more complex breathing patterns based on its outputs.

That other approaches for complex breathing pattern classification can be contributed by other groups and that they can be compared in a standardized way, the presented data set is published. Expanding the data set to include other breathing patterns that occur, for example, in obstructive, or restrictive lung diseases, would also be an interesting prospect for subsequent work, which could further increase the medical usability of the classification results. In a larger patient study in the recovery room of the RWTH Aachen University Hospital, the results of the presented subject study are currently being compared and validated with actual pathological breathing patterns. This shall ensure that both the data set and the developed classifiers are suitable for practical use.

**Funding:** This research was funded by the German Federal Ministry of Education and Research grant number 13N14772.

**Ethics:** The experiments were conducted with the help of volunteering colleagues. According to the ethics committee of the medical faculty of the RWTH Aachen University, Germany, therefore, no ethics approval was necessary. Informed consent was obtained from all subjects involved in the study.

**Acknowledgments:** The authors thank all colleagues, which volunteered in this study for their time and their excellent breathing patterns.

**Conflicts of Interest:** The authors declare no conflict of interest.

**Abbreviations:** The following abbreviations are used in this manuscript:

<b>CWT</b> Continuous Wavelet Transform. 7–9, 15, 17	<b>RMSE</b> Root Mean Square Error. 9, 11, 12
<b>FFT</b> Fast Fourier Transform. 6	<b>RoI</b> Region of Interest. 5, 9, 11, 14
<b>IRT</b> Infrared Thermography. 2–5, 9, 11, 13, 14	<b>RR</b> Respiratory Rate. 2, 3, 6–9, 11, 13, 15
<b>KLT</b> Kanade-Lucas-Tomasi. 4, 5	<b>SVD</b> Singular value decomposition. 4
<b>NIR</b> Near Infrared. 2	<b>SVM</b> Support Vector Machine. 9
<b>PCA</b> Principal component analysis. 5, 6, 15	<b>WFDB</b> Waveform Database. 6
<b>RE</b> Respiratory Effort. 2, 3, 6, 9, 11, 13–15	

## A Experimental setup

Table 5: Devices used for data caption

Device	Product Name	Manufacturer	Information
Chest Sensor	PVDF Effort Sensor	SleepSense	
Adbodem Sensor	PVDF Effort Sensor	SleepSense	
A/D Converter	NI USB-6008	Nordic Instruments	resolution: 12 bit, sampling rate: 5 kHz
Ring Light	SL-480	Dörr	color temperature: 4600 K, illumination power: 1000 lx
RGB-Camera	Mako G234C	Allied Vision	resolution: 1920 x 1080 px, color depth: 8 bit, frame rate: 15 FPS lens: Kowa LM50HC
Thermal camera	Boson 640	FLIR	resolution: 640 x 512 px, color depth: 16 bit, frame rate: 30 FPS, lens: 12°C FOV spectral range: 7,5 - 13,5 $\mu\text{m}$

Table 6: Pattern description of the breath-protocol, shown in Figure 3

No.	Pattern	Frequency Breaths/min	Effort norm. units units	Targ. Range Breaths/min
1	Bradypnea	5	1	5 - 10
2	Eupnea	12	1	12 - 18
3	Hypopnea	12	0.25	12 - 18
4	Hyperpnea	10	2.5	12 - 18
5	Tachypnea	35	1	20 - 35
6	Eupnea	15	1	12 - 25
7	Kussmaul breathing	30	2.5	20 - 35
8	Cheyne-Stokes respiration	0, 20	0-4.5	12 - 25
9	Tachypnea	35	0.25	20 - 35
10	Biot's breathing	0, 15	1	12 - 25
11	Biot's breathing	0, 10	2.5	12 - 25
12	Apnea	0	0	0

## B Used Parameters

Table 7: Parameters for Savitzky Golay pre-processing filter

Order	Frame length
2	1.5 s

Table 8: Parameters for the Peak detection algorithm

Prominence	Min. Distance	Max. Peak width
0.3 n.u.	$\frac{60 \text{ s min}^{-1}}{40 \text{ Breaths/min}} = 1.5 \text{ s}$	$\frac{2}{3} \frac{60 \text{ s min}^{-1}}{4 \text{ Breaths/min}} = 10 \text{ s}$

Table 9: Parameters for the CWT

Wavelet	Time-Bandwidth product	Voices per octave	Frequency range
Morse	10	48	[440]Breaths/min = [0.0670.667]Hz

## References

- [1] Jasmeet Soar, Ian Maconochie, Myra H. Wyckoff, Theresa M. Olasveengen, Eunice M. Singletary, et al. 2019 International Consensus on Cardiopulmonary Resuscitation and Emergency Cardiovascular Care Science With Treatment Recommendations: Summary From the Basic Life Support; Advanced Life Support; Pediatric Life Support; Neonatal Life Support; Education, Implementation, and Teams; and First Aid Task Forces. *Circulation*, 140(24), December 2019. ISSN 0009-7322, 1524-4539. doi:10.1161/CIR.0000000000000734.
- [2] The ATLS Subcommittee, American College of Surgeons' Committee on Trauma, and the International ATLS working group. Advanced trauma life support (ATLS®): The ninth edition. *Journal of Trauma and Acute Care Surgery*, 74(5):1363–1366, May 2013. ISSN 2163-0755. doi:10.1097/TA.0b013e31828b82f5.
- [3] Troels Thim, Krarup, Grove, Rohde, and Lofgren. Initial assessment and treatment with the Airway, Breathing, Circulation, Disability, Exposure (ABCDE) approach. *International Journal of General Medicine*, page 117, January 2012. ISSN 1178-7074. doi:10.2147/IJGM.S28478.
- [4] F.Q. AL-Khalidi, R. Saatchi, D. Burke, H. Elphick, and S. Tan. Respiration rate monitoring methods: A review: Respiration Rate Monitoring Methods. *Pediatric Pulmonology*, 46(6):523–529, June 2011. ISSN 87556863. doi:10.1002/ppul.21416.
- [5] Mubashir Rehman, Raza Ali Shah, Muhammad Bilal Khan, Syed Aziz Shah, Najah Abed AbuAli, Xiaodong Yang, Akram Alomainy, Muhmmad Ali Imran, and Qammer H. Abbasi. Improving Machine Learning Classification Accuracy for Breathing Abnormalities by Enhancing Dataset. *Sensors*, 21(20):6750, October 2021. ISSN 1424-8220. doi:10.3390/s21206750.
- [6] Chiara Romano, Emiliano Schena, Sergio Silvestri, and Carlo Massaroni. Non-Contact Respiratory Monitoring Using an RGB Camera for Real-World Applications. *Sensors*, 21(15):5126, July 2021. ISSN 1424-8220. doi:10.3390/s21155126.
- [7] Carina Barbosa Pereira, Xinchu Yu, Michael Czaplik, Vladimir Blazek, Boudewijn Venema, and Steffen Leonhardt. Estimation of breathing rate in thermal imaging videos: A pilot study on healthy human subjects. *Journal of Clinical Monitoring and Computing*, 31(6):1241–1254, December 2017. ISSN 1573-2614. doi:10.1007/s10877-016-9949-y.
- [8] Lacey Whited and Derrel Graham. Abnormal Respirations. Available online: <https://www.ncbi.nlm.nih.gov/books/NBK470309/> (accessed on 2022-09-07). (accessed 2022-09-07).
- [9] Ralf Brandes, Florian Lang, and Robert F. Schmidt, editors. *Physiologie des Menschen: mit Pathophysiologie*. Springer-Lehrbuch. Springer Berlin Heidelberg, Berlin, Heidelberg, 2019. ISBN 978-3-662-56467-7 978-3-662-56468-4. doi:10.1007/978-3-662-56468-4.
- [10] Paul E.H. Ricard. Pulmonary System. In *Acute Care Handbook for Physical Therapists*, pages 53–83. Elsevier, 2014. ISBN 978-1-4557-2896-1. doi:10.1016/B978-1-4557-2896-1.00004-4.
- [11] Lorena Olivencia Peña, María Sevilla Martínez, and Alberto Fernández Carmona. Spontaneous Breathing Pattern. In Antonio M. Esquinas and Nicola Vargas, editors, *Ventilatory Support and Oxygen Therapy in Elder, Palliative and End-of-Life Care Patients*, pages 3–13. Springer International Publishing, Cham, 2020. ISBN 978-3-030-26664-6. doi:10.1007/978-3-030-26664-6\_1.
- [12] Atemfrequenz - Wikipedia, die freie Enzyklopädie. Available online: <https://de.wikipedia.org/w/index.php?title=Atemfrequenz&oldid=212158595> (accessed on 2022-09-14). (accessed 2022-09-14).
- [13] Kussmaul. Zur Lehre vom Diabetes Mellitus. *Deutsches Archiv für klinische Medizin*, 14:1–47, August 1874.
- [14] Cleve Moler. MATLAB 2022a. The Mathworks Inc., 2022.
- [15] Jianbo Shi and Tomasi. Good features to track. In *Proceedings of IEEE Conference on Computer Vision and Pattern Recognition CVPR-94*, pages 593–600, Seattle, WA, USA, 1994. IEEE Comput. Soc. Press. ISBN 978-0-8186-5825-9. doi:10.1109/CVPR.1994.323794.

- [16] Bruce D. Lucas and Takeo Kanade. An Iterative Image Registration Technique with an Application to Stereo Vision. In *Proceedings of the 7th International Joint Conference on Artificial Intelligence - Volume 2*, IJCAI'81, pages 674–679, San Francisco, CA, USA, 1981. Morgan Kaufmann Publishers Inc.
- [17] Carlo Tomasi and Takeo Kanade. Detection and Tracking of Point Features. Technical Report CMU-CS-91-132, Carnegie Mellon University, Pittsburgh, April 1991.
- [18] Carina Barbosa Pereira, Xinchu Yu, Michael Czaplak, Rolf Rossaint, Vladimir Blazek, and Steffen Leonhardt. Remote monitoring of breathing dynamics using infrared thermography. *Biomedical Optics Express*, 6(11):4378, November 2015. ISSN 2156-7085, 2156-7085. doi:10.1364/BOE.6.004378.
- [19] Carina B. Pereira, Xinchu Yu, Vladimir Blazek, and Steffen Leonhardt. Robust remote monitoring of breathing function by using infrared thermography. In *2015 37th Annual International Conference of the IEEE Engineering in Medicine and Biology Society (EMBC)*, pages 4250–4253, Milan, August 2015. IEEE. ISBN 978-1-4244-9271-8. doi:10.1109/EMBC.2015.7319333.
- [20] K. Mutlu, J. Esquivelzeta Rabell, P. Martin del Olmo, and S. Haesler. IR thermography-based monitoring of respiration phase without image segmentation. *Journal of Neuroscience Methods*, 301:1–8, May 2018. ISSN 01650270. doi:10.1016/j.jneumeth.2018.02.017.
- [21] Nobuyuki Otsu. A Threshold Selection Method from Gray-Level Histograms. *IEEE Transactions on Systems, Man, and Cybernetics*, 9(1):62–66, January 1979. ISSN 0018-9472, 2168-2909. doi:10.1109/TSMC.1979.4310076.
- [22] Abraham. Savitzky and M. J. E. Golay. Smoothing and Differentiation of Data by Simplified Least Squares Procedures. *Analytical Chemistry*, 36(8):1627–1639, July 1964. ISSN 0003-2700, 1520-6882. doi:10.1021/ac60214a047.
- [23] Mallat Stéphane. Time Meets Frequency. In *A Wavelet Tour of Signal Processing*, pages 89–153. Elsevier, 2009. ISBN 978-0-12-374370-1. doi:10.1016/B978-0-12-374370-1.00008-2.
- [24] Wapnik and Chervonenkis. Theory of Pattern Recognition. 1974.
- [25] Trevor Hastie and Robert Tibshirani. Classification by pairwise coupling. *The Annals of Statistics*, 26(2):451–471, April 1998. doi:10.1214/aos/1028144844.